High Power Laser Science and Engineering, (2023), Vol. 11, e15, 9 pages.
doi:10.1017/hpl.2022.41

HIGH POWER LASER SCIENCE AND ENGINEERING

RESEARCH ARTICLE

Impact of temporal modulations on laser-induced damage of fused silica at 351 nm

C. Bouyer[1], R. Parreault[1], N. Roquin[1], J.-Y. Natoli[2], and L. Lamaignère[1]

[1]*CEA CESTA, Le Barp, France*

[2]*Aix-Marseille Univ, CNRS, Centrale Marseille, Institut Fresnel, Marseille, France*

(Received 29 August 2022; revised 27 October 2022; accepted 12 December 2022)

Abstract

Laser-induced damage (LID) on high-power laser facilities is one of the limiting factors for the increase in power and energy. Inertial confinement fusion (ICF) facilities such as Laser Mégajoule or the National Ignition Facility use spectral broadening of the laser pulse that may induce power modulations because of frequency modulation to amplitude modulation conversion. In this paper, we study the impact of low and fast power modulations of laser pulses both experimentally and numerically. The MELBA experimental testbed was used to shape a wide variety of laser pulses and to study their impact on LID. A 1D Lagrangian hydrodynamic code was used to understand the impact of different power profiles on LID.

Keywords: fused silica; high-power laser; laser diagnostics; laser-induced damage

1. Introduction

Laser-induced damage (LID) is one of the most limiting phenomena for the increase of overall energy and peak power for high-power laser facilities, such as the National Ignition Facility (NIF)[1] or Laser Mégajoule (LMJ)[2]. As far as LMJ is concerned, the resistance of optics to LID is qualified in support laboratories with specific lasers. The latter are not necessarily representative of LMJ pulses as they are often small beams of a few 100 μm of diameter with temporal Gaussian shapes at a fixed pulse duration. By comparison, typical beam sizes at LMJ are equal to 1600 cm^2, for which the temporal profile varies both in shape and duration. A temporal scaling law[3,4] is then used to assess the performance of LMJ optics from the results obtained in support laboratories.

At NIF and LMJ, the temporal shape may vary from one experiment to another. Indeed, some experiments may require a progressive laser energy deposit on target while other experiments for the study of shocks may require pulses for which the energy is suddenly delivered. Another issue concerning high-power nanosecond lasers is the indirect effect of phase modulations used at NIF and LMJ to tackle the issues of Brillouin scattering[5] and optical smoothing[6]. Such phase modulations have the effect of broadening the optical spectrum of laser pulses. When propagating along the beamline, the optical spectrum of the laser pulse may be distorted by several processes. This induces amplitude modulations (AMs) on an initially temporally smooth laser pulse. This effect is called frequency modulation to amplitude modulation (FM-to-AM) conversion[7,8]. Nowadays, such an effect is not considered to predict laser damage. One can hypothesize *a priori* that fast power variations induced by FM-to-AM conversion can have a strong impact on the absorption of subsurface damage (SSD) that leads to LID[9]. For instance, previous work[10] showed that multi-longitudinal mode (MLM) laser pulses with high-frequency (HF) power modulation can increase the LID threshold of fused silica at 351 nm, when compared to a temporally smooth monomode laser pulse.

Our goal throughout this paper is to study the impact of power modulations with FM-to-AM conversion characteristics on the LID of fused silica in the ultraviolet (UV) range at 351 nm. Thanks to amplitude modulators that are able to scan a wide amplitude and frequency range, several experiments were done on the MELBA experimental testbed to assess the impact of different temporal profiles of the laser pulse on LID.

To go further, a 1D Lagrangian hydrodynamic code was used to run simulations and explain the LID discrepancies observed experimentally with different temporal profiles. The aim is to gauge the impact of the power modulations

Correspondence to: C. Bouyer, CEA CESTA, F33116 Le Barp, France.
Email: charles.bouyer@cea.fr

on the absorption of SSD leading to the creation of laser damage.

2. Experimental setup for the study of laser-induced damage

2.1. Description of the MELBA experimental testbed

Reported experiments were carried out on the MELBA[11] experimental testbed located at CEA CESTA (France). Initially, a 1053 nm laser pulse (1ω pulse) is created in a master oscillator with an energy of the order of nJ and a pulse duration of 200 ns. A phase modulation is applied at 2 GHz to prevent stimulated Brillouin scattering during laser propagation. Then, the pulse is amplified through a fiber amplifier.

Two all-fiber Mach–Zehnder interferometers are used to shape the temporal profile of the laser pulse. The first interferometer outputs the user-defined laser pulse. The second interferometer improves the extinction ratio. The overall extinction ratio at the output of both Mach–Zehnder interferometers is 52 dB. For instance, it is possible to create flat-in-time (FIT) or Gaussian pulses of different pulse durations. In fact, the user can program any laser pulse with a temporal resolution of approximately 100 ps and a maximum pulse duration of approximately 20 ns.

To apply fast temporal modulations to the laser pulse and recreate the impact of FM-to-AM conversion on the temporal profile, an all-fiber electro-optic amplitude modulator with a 40 GHz bandwidth was set up. The amplitude modulator can be coupled to two different radio frequency (RF) drivers:

- a low-frequency (LF) four-channel RF driver generating signals at 2, 4, 6 and 8 GHz adjustable in amplitude and phase;
- an HF three-channel RF driver generating signals at 10, 20 and 30 GHz adjustable in amplitude and phase.

The expression of the laser power P at the output of the modulator is expressed as follows:

$$P(t) = \frac{P_0(t)}{2}\left(1+\sin\left(\sum_{k=1}^{N_{\mathrm{CH}}}\frac{V_k}{V_{\pi,k}}\pi\sin\left(2\pi k f_0 t+\varphi_k\right)\right)\right), \tag{1}$$

where N_{CH} is the total number of channels, which depends on the RF driver. The LF driver has $N_{\mathrm{CH}}=4$ while the HF driver has $N_{\mathrm{CH}}=3$. In the equation, P_0 is the power at the input of the modulator, V_k is the voltage input of channel k and $V_{\pi,k}$ is the voltage of channel k required to induce a phase shift of π radians. Finally, $f_0=2$ or 10 GHz depending on the driver and φ_k is the phase shift applied to channel k. The idea behind using an amplitude modulator instead of directly inducing FM-to-AM conversion is twofold: better control of the temporal profile and the generation of modulation frequencies with limited harmonics[7] that are adapted to measurement bandwidths. Temporal measurements at 351 nm are carried out with 40 GHz fiber-coupled photodiodes connected to a 33 GHz oscilloscope. Thus, the overall bandwidth is 33 GHz.

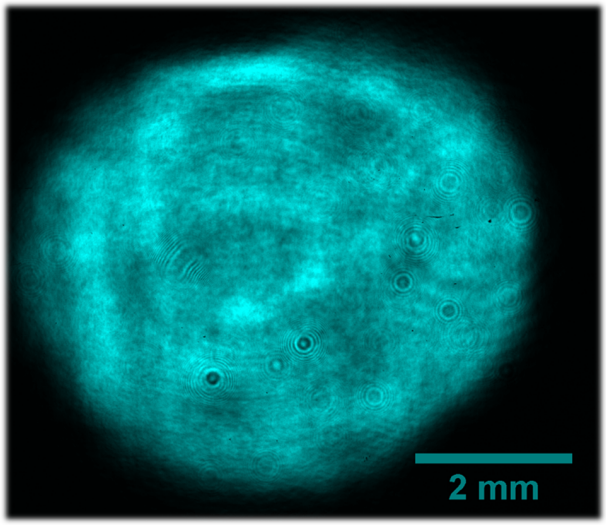

Figure 1. MELBA 3ω spatial profile on the fused silica sample.

After applying temporal pulse shaping, the laser pulse is amplified through a regenerative amplifier to approximately 10 mJ. Then, a four-pass amplifier followed by two booster amplifiers bring the energy up to 7 J. The laser pulse is converted in the UV range at 351 nm (3ω pulse) thanks to two lithium triborate (LBO) crystals in a type-I type-II configuration. Typical 3ω energies are around 3 J. A lens focuses the laser on the silica sample under study. The sample is located at an intermediary field, so the diameter of the beam is approximately 6 mm with a top-hat spatial shape. Figure 1 represents the fluence profile of the 3ω beam incident of the sample test. Many high-end diagnostics, which will be presented subsequently, allow us to properly measure all laser parameters needed for the experiments.

2.2. Studying LID on the MELBA experimental testbed

The MELBA experimental testbed is used to study LID and laser damage growth. The analysis of LID on a given test site is composed of several steps. Firstly, the test site of a superpolished synthetic fused silica sample is irradiated with the 3ω beam. Then, the detection of LID is made thanks to a macroscope that is inserted after each shot. The photography taken by the macroscope is binarized. The fluence profile is determined thanks to a charge-coupled device (CCD) camera with a 1392×1040 pixels large sensor and a pixel area of $6.45\ \mu\mathrm{m} \times 6.45\ \mu\mathrm{m}$. The local fluence for each pixel is calculated by normalizing the integral of the image to the energy measured by diagnostics for the shot. Each damage is treated as an object and the local fluence at which it is triggered is stored as data.

https://doi.org/10.1017/hpl.2022.41 Published online by Cambridge University Press

With enough tested sites, we can determine damage densities ρ (cm^{-2}) for given fluence ranges F_k (J cm^{-2}) thanks to the following formula:

$$\rho(F_k) = \frac{N_{\text{dam}}(F_k)}{S_{\text{px}} N_{\text{px}}(F_k)}, \tag{2}$$

with N_{dam} being the number of damage sites for all fluences in range F_k, N_{px} being the number of illuminated CCD pixels for all fluences in the range F_k and S_{px} being the surface of a pixel. A damage law is defined as being the collection of all damage densities $\rho(F_k)$ determined on all tested sites. Every damage law comparison is carried out on a dedicated silica sample. This allows us to compare the impact of different pulses on LID with the same sample quality.

Statistical error bars are calculated with the collected damage densities and a histogram[12], for each fluence range F_k. Fluence error bars are usually in the 10%–15% range[13].

2.3. Characterization of the temporal profile

Damage laws determined with different pulse shapes will be compared to each other, all else being equal. This includes the fact that pulses will have the same pulse duration τ_{eff}. As described in the ISO standard[14] for laser damage, we will use the effective pulse duration to compare different pulses. It is determined via the following formula:

$$\tau_{\text{eff}} = \frac{\int P(t)\mathrm{d}t}{\max P(t)} = \frac{E}{\max P(t)}, \tag{3}$$

where $P(t)$ is the power profile, $\max P(t)$ is the peak power reached and E is the energy of the pulse. Then, the magnitude of AM is defined thanks to modulation index β as follows:

$$\beta = \frac{\max P(t)}{\langle P(t) \rangle} - 1. \tag{4}$$

For instance, a modulation index of 100% means that the AMs reach two times the mean power of the pulse. A representation of temporally modulated pulses will be presented later in Section 3.1. Note that in this paper, the effective pulse duration computation does not take the AM into account. It is solely the envelope (or unmodulated pulse) that is used to determine τ_{eff}. If we did not take this into consideration, an increase of β would directly lead to a decrease in the effective pulse duration.

3. Impact of temporal modulations on laser-induced damage

3.1. Temporal characteristics of LF and HF laser pulses

Due to the spectral broadening of laser pulses, high-power facilities such as LMJ or NIF deliver pulses that may undergo FM-to-AM conversion. This phenomenon is responsible for power modulations of different magnitudes and frequencies. As previously discussed, we can reproduce such modulations on the MELBA testbed thanks to LF and HF modulators. Several AM configurations were used to assess the impact of LF and HF modulations, as follows.

- An FIT reference case with an effective pulse duration of 4 ns.
- Three amplitude modulated pulses at 2 GHz with modulation indices $\beta_{2\text{GHz}} = 55\%, 110\%, 130\%$. The envelope is an FIT pulse of effective pulse duration equal to 4 ns.
- Two amplitude modulated pulses at 10 GHz with modulation indices $\beta_{10\text{GHz}} = 55\%, 95\%$. The envelope is an FIT pulse of effective pulse duration equal to 4 ns.
- An amplitude modulated pulse at 30 GHz with a modulation index $\beta_{30\text{GHz}} = 91\%$. The envelope is an FIT pulse of effective pulse duration equal to 4 ns.

The reference FIT pulse as well as different modulated pulses is presented in Figure 2(a). Power profiles are normalized so that the average power is equal to 1. As several sites are tested for each configuration, the calculated modulation index varies from site to site. The presented modulation index is the average modulation index for all tested sites of a given configuration. Relative standard deviations for all modulated configurations comprise between 5 and 11 percentage points.

Figure 2(a) shows the amplitude of the Fourier transform of the pulses presented in Figure 2(a). For the 2 GHz configuration, we can detect harmonics up to 8 GHz, but these harmonics are quite low when compared to the fundamental at 2 GHz. The 10 GHz configuration only shows the fundamental at 10 GHz, without any noticeable upper harmonics. Finally, the 30 GHz configuration only shows a distinctive peak at 30 GHz, as the bandwidth is limited to 33 GHz. Complementary measurements with a streak camera at 3ω showed that some shots exhibited an upper harmonic at 60 GHz, but with a low peak amplitude.

3.2. Comparison of damage laws for LF and HF modulated pulses

Four different temporal profiles were considered to test the impact of LF modulations on LID: a reference case and three 2 GHz modulated pulses of increasing modulation indices $\beta_{2\text{GHz}} = 55\%, 110\%, 130\%$. The silica sample used for the test was polished by the THALES-SESO company with a thickness of 10 mm. Results of these test procedures are presented in Figure 3(a). Damage laws show that LF power modulations at 2 GHz give noticeably different damage densities in the 15–30 J cm^{-2} fluence range, well beyond error bars. Indeed, damage densities for modulated pulses are systematically above the reference FIT case. Moreover, the higher the modulation index, the greater this difference

https://doi.org/10.1017/hpl.2022.41 Published online by Cambridge University Press

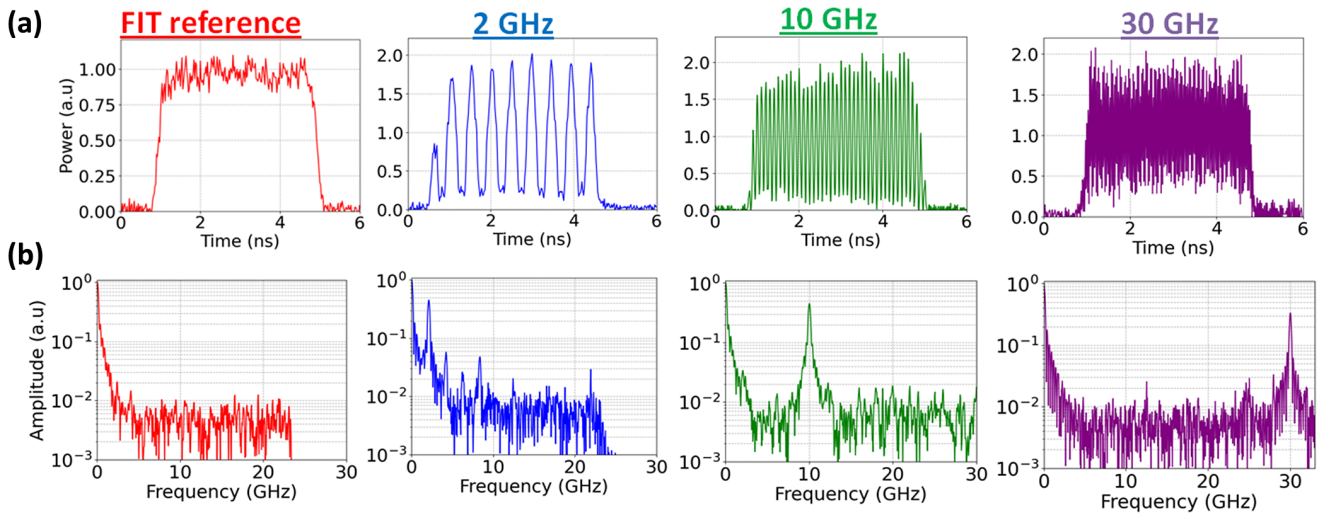

Figure 2. (a) Examples of power profiles measured with a 33 GHz-bandwidth oscilloscope and photodiode. From left to right: FIT reference and 2, 10 and 30 GHz pulses. The modulation index is approximately equal to 100% for modulated pulses. Power profiles are normalized so that the average power is equal to 1. (b) The amplitude of the Fourier transform for each power profile shown in (a).

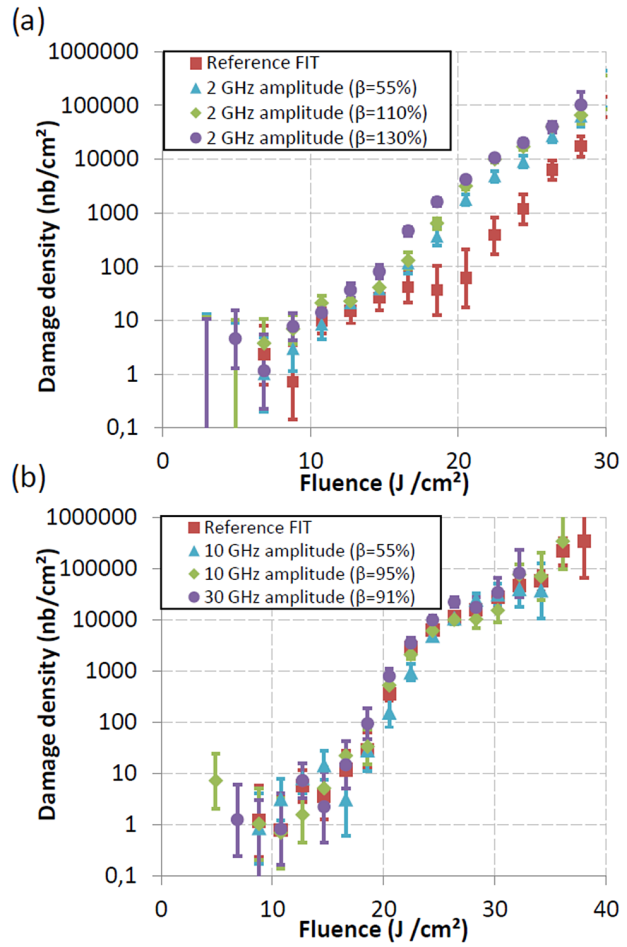

Figure 3. (a) Damage laws for the FIT reference pulse and three 2 GHz pulses of different modulation indices. (b) Damage laws for the FIT reference case, two 10 GHz pulses with different modulation indices and a 30 GHz pulse.

is. In the worst case, we observe a difference in laser damage density between 10 and 100 times when comparing the reference FIT pulse and the 2 GHz pulse with $\beta_{2\text{GHz}} = 130\%$.

In order to assess the impact of the frequency of AMs, tests were performed with HF AMs on another 10 mm thick silica sample polished by THALES-SESO. Again, four different configurations were tested: a smooth reference FIT power profile, two 10 GHz modulated power profiles ($\beta_{10\text{GHz}} = 55\%$ and $\beta = 95\%$) and a 30 GHz modulated power profile with $\beta_{30\text{GHz}} = 91\%$. HF power modulations were achieved thanks to the HF channel modulator of the MELBA experimental testbed. Damage laws obtained for these four configurations are presented in Figure 3(b). For HF modulations, the experimental results clearly show that the damage laws are the same for a large range of frequencies (10–30 GHz) and different values of modulation indices (from $\beta = 55\%$ to $\beta = 95\%$).

A final test was carried out on a new fused silica sample, which was provided by another vendor, namely the ZYGO company. The thickness of the sample is the same as the THALES-SESO sample, namely 10 mm. A damage law for a reference FIT pulse profile was first determined. Then, we tested for two different modulation amplitudes representative of LF and HF power modulations, namely a 2 GHz modulated pulse ($\beta = 122\%$) and a 10 GHz modulated pulse ($\beta = 117\%$). The results are presented in Figure 4. We observe tendencies similar to those presented in Figure 3. Indeed, LF AMs (2 GHz) lead to higher damage densities when compared to the reference FIT case. Moreover, there is no noticeable difference between the reference and the 10 GHz damage laws. In contrast with the results presented in Figure 3, we notice that the fluence values for which we observe a difference between the reference and the 2 GHz damage laws are between 10 and 25 J cm^{-2}.

https://doi.org/10.1017/hpl.2022.41 Published online by Cambridge University Press

Comparison of the size damage sites for the experiment presented in Figure 4 is shown in Figure 5. The results show no dependence of the temporal profile on damage size. This means that AMs at 2 or 10 GHz do not have an influence on laser damage size, when compared to the unmodulated reference pulse. As far as damage morphology is concerned, we did not find any difference between damage sites originating from different temporal profiles. This is coherent with work from Chambonneau *et al.*[15] and Diaz *et al.*[10], which showed no important damage morphology change between unmodulated and modulated 3ω pulses.

Moreover, work from Diaz *et al.*[10] showed that pulses with AM gave different damage laws at 3ω when compared to a smooth reference case. In their work, damage densities determined with an MLM pulse of very high peak power and high frequencies are lower than those obtained with a smooth single-longitudinal mode (SLM) pulse. This result is difficult to compare to ours, as MLM pulses vary a great deal from shot to shot and span a much greater range of frequencies[16]. Nevertheless, it still shows that amplitude modulated pulses can lead to different damage laws.

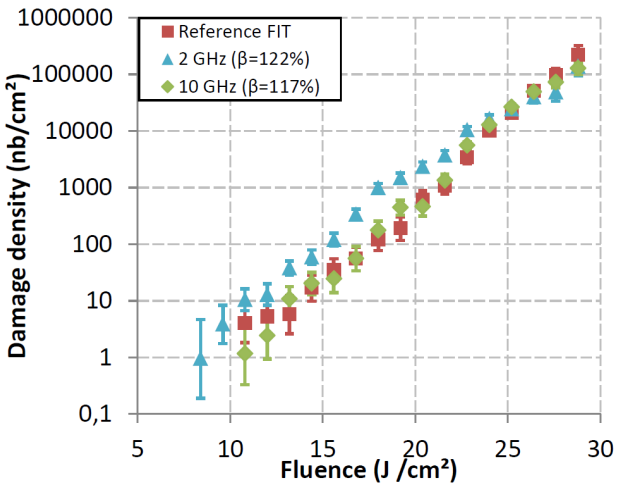

Figure 4. Damage laws determined on a fused silica sample polished by another vendor (reference FIT pulse, 2 GHz modulation and 10 GHz modulation).

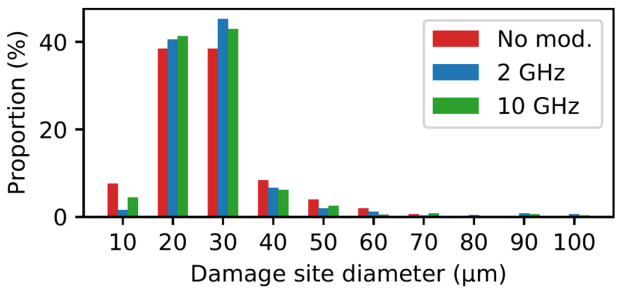

Figure 5. Histogram of the damage site diameter for the reference unmodulated pulse (no mod.) and the two amplitude modulations at 2 and 10 GHz. Data were analyzed from the results of the experiment presented in Figure 4.

To explain the tendencies we observed experimentally, a model of laser–matter interaction was developed to assess the impact of AMs on the LID of fused silica at 351 nm. A description of the model and the results are presented in the following section.

4. A model to understand laser-induced damage with Esther code

4.1. Description of the model

Amorphous silica can be modeled with a band structure, with a gap between the conduction and valence bands equal to 8.825 eV. This energy gap is approximately three times the energy of a UV photon at 351 nm (3.52 eV). Yet, laser damage is observed despite the transparency of amorphous silica to UV light. The triggering of laser damage in fused silica is mainly explained by single-photon absorption of the incoming laser energy by SSD. Such defects are most often considered to be either absorbing pollutant particles or micro-cracks originating from the polishing process. In the context of the LMJ facility, the quality of silica optics is such that most absorbing pollutants particles should disappear with an etching process[17]. Thus, we will consider subsurface micro-cracks as being the sole contributor to laser damage. The model was designed similarly to the model used by Diaz *et al.*[10] and Grua *et al.*[4]. The outline representing the model is represented in Figure 6.

The crack is modeled by a 100 nm void surrounded by amorphous silica. At the interface, the silica can absorb part of the laser energy due to the presence of an arbitrary absorbing defect layer. Examples of such defects can be found in Ref. [18]. Dimension L is considered much greater than dimension x, as shown on the outline in Figure 6. Thus,

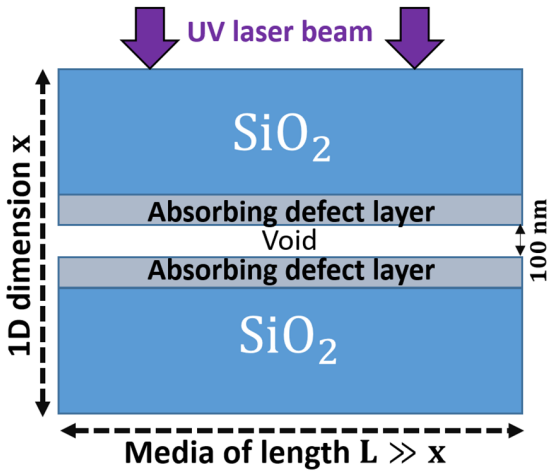

Figure 6. Outline of the modeling of subsurface micro-cracks. The crack is modeled by a 100 nm void surrounded by amorphous silica. Absorption of the UV laser at the SiO_2/void interface is represented by an arbitrary absorbing defect layer.

https://doi.org/10.1017/hpl.2022.41 Published online by Cambridge University Press

the model is 1D along x with planar symmetry. Physical processes that may occur during laser absorption by fused silica are modeled via a 1D Lagrangian thermo-mechanical model coupled to Helmholtz equations for the propagation of electromagnetic waves in different media. The choice for the equation of state (EOS) of fused silica is detailed in Ref. [4]. The model is solved numerically thanks to the Esther[19] code developed by CEA, which focuses on laser–matter interaction. The key factors to consider for such a modeling are the surface absorptivity of the absorbing defect as well as the evolution of the absorptivity of fused silica as a function of the density ρ and temperature T of fused silica. At temperatures below 2000–3000 K, the silica typically remains isochoric and only its temperature increases with energy deposits[19]. We provide the numerical code with values for the imaginary refractive index n'' of silica as a function of temperature with the Urbach rule[4,20]:

$$n''(T) = \frac{\lambda}{4\pi}\alpha_0 \exp\left(\sigma_0 \frac{hf - E_g}{k_B T}\right), \tag{5}$$

with $hf = 3.52$eV being the energy of photons at 351 nm and $E_g = 8.825$eV being the band gap for amorphous silica. Other constants are $\alpha_0 = 4.095 \times 10^{-7}$ m^{-1} and $\sigma_0 = 0.0455$.

As the temperature of the fused silica T rises, so does the imaginary index of refraction as $\exp(-1/T)$. When the temperature increases beyond 2000–3000 K, fused silica tends to become strongly absorbent[21]. For these high temperatures, the Drude model is preferred[4]. The expression for the permittivity for fused silica used in the code, the function of density ρ and temperature T are as follows:

$$\varepsilon(T,\rho) = 1 + i\frac{\sigma_0(T,\rho)}{\varepsilon_0 \omega}\left(1 - i\frac{\omega m_e M_{SiO_2}\sigma_0(T,\rho)}{N_A \rho Z(T,\rho) e^2}\right)^{-1}. \tag{6}$$

In the equation above, ω is the laser angular frequency, $\varepsilon_0 = 8.85 \times 10^{-12}$ F m^{-1} is the vacuum permittivity, N_A is the Avogadro constant, $M_{SiO_2} = 60.1$ g mol^{-1} is the molar mass of fused silica, $e = -1.60 \times 10^{-19}$ C is the elementary charge and $m_e = 9.11 \times 10^{-31}$ kg is the electron mass. Continuous electrical conductivity $\sigma_0(T,\rho)$ is determined thanks to the mixing of SCAALP[22,23] (self-consistent average-atom model for laboratory plasmas) data of oxygen (2 atoms) and silicon (1 atom). The ionization $Z(T,\rho)$ is used from internal data and is based on a Thomas–Fermi model with gap[24]. Heat transport is also computed from the SCAALP data of oxygen and silicon.

The initial temperature increase is exclusively driven by the surface absorptivity of the arbitrary absorbing defect. We chose an imaginary refractive index for the absorbing defect of 10^{-3} because it leads to the apparition of a laser damage for fluences between 20 and 35 J cm^{-2}, depending on laser input when solving numerically. These fluences agree with the experimental fluences for which we observed LID.

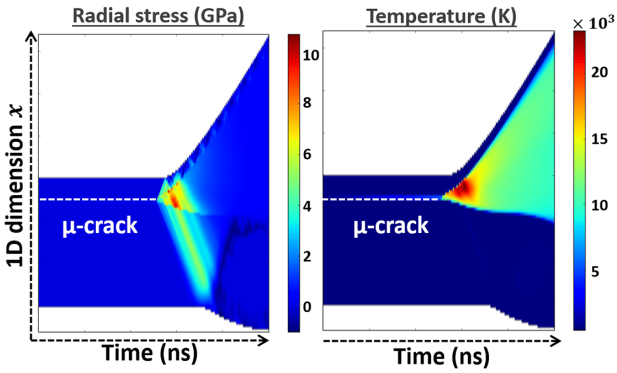

Figure 7. Radial stress and temperature output of the code with respect to time and the 1D parameter x.

The thickness of these layers is 5 nm. This choice is made because such defects are localized at the surface interface of the void and silica, so the thickness must be as low as possible. To optimize the calculation time, the meshing of silica follows a geometric progression that provides a fine meshing close to the micro-crack and a rougher meshing far from it. The temporal step for calculation is adapted to the AM frequency of the tested power profile.

The main output parameters considered to track the laser-induced damage threshold (LIDT) for different temporal configurations are the radial stress reached within the material and the temperature. An example for data output of the Esther code is presented in Figure 7. Criteria for laser damage are chosen when the maximal radial stress exceeds the tensile strength of fused silica, which is equal to 50 MPa. Our criteria for LIDT are chosen at 1 GPa. This is because we want to be sure that the damage phenomenon has occurred. In fact, the results of simulations presented in the following section show that the choice for the damage stress criteria has a weak influence for determining the LIDT, as the radial stress strongly increases with the fluence of the laser.

4.2. *How to compare the LIDT and damage laws*

On the one hand, simulations carried out with Esther code will give information about the fact that a given defect will lead to LID. The fluence at which damage occurs will be called the LIDT. On the other hand, damage laws determined experimentally give a set of damage densities as a function of fluence. Thus, the comparison of experimental and simulated results requires the possibility of defining an LIDT from a damage law. Given a damage law, the following applies.

(1) An arbitrary damage density is fixed and defines the value for which we consider LID.

(2) From the damage law, we define the fluence for which the associated damage density is equal to the value determined in (1). This is the LIDT.

https://doi.org/10.1017/hpl.2022.41 Published online by Cambridge University Press

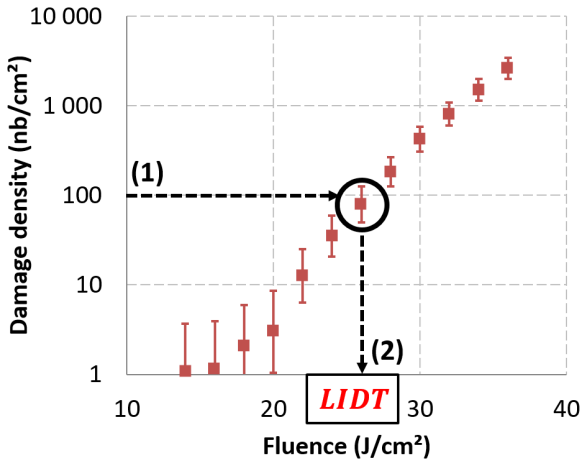

Figure 8. Determination of the laser-induced damage threshold (LIDT) from a damage law, given a damage density threshold defined at 100 nb/cm^2.

Figure 8 represents the method used to associate an LIDT from a given damage law determined experimentally.

4.3. Simulations and comparison to experimental results

Pulses with AMs at 2, 10 and 30 GHz with $\beta = 100\%$ were tested with our model. An additional modulated pulse at 2 GHz with $\beta = 50\%$ was also used in our simulations to assess the impact of the modulation index β. Results for the maximal radial stress reached inside the micro-crack with respect to fluence are presented in Figure 9. Simulations associated with modulated pulses are compared to a reference FIT pulse without modulations.

Firstly, we notice that modulations at 2 GHz ($\beta = 100\%$) give an LIDT at a lower fluence when compared to the reference FIT pulse. The LIDT associated with the 2 GHz modulated pulse with $\beta = 50\%$ is lower than the reference, but this difference is smaller than in the $\beta = 100\%$ case. Both of these results are in good agreement with the tendencies observed experimentally in Figures 3(a) and 4.

Concerning the modulated pulse at 10 GHz with $\beta = 100\%$, the LIDT is the same as the reference FIT case. Simulations are coherent with the experimental results obtained in Figures 3(b) and 4.

When the modulation frequency is equal to 30 GHz ($\beta = 100\%$), the simulated LIDT is slightly superior to the LIDT of the unmodulated reference FIT case. Nevertheless, this difference is smaller than that of the 2 GHz ($\beta = 100\%$) LIDT and the unmodulated reference LIDT. Thus, we can consider that the 30 GHz LIDT is closer to the reference case than the 2 GHz LIDT. This result is coherent with those obtained in Figure 3(b).

To understand the difference in simulated LIDT for modulated pulses, it is interesting to look at the evolution of thermodynamic parameters with respect to time. Figure 10 shows the evolution of temperature reached within the micro-crack for the reference FIT case (no mod.) and two modulated pulses with $\beta = 100\%$ at 2 and 10 GHz. The chosen fluence for the simulation corresponds to the LIDT of the unmodulated and the 10 GHz pulse (25 J cm^{-2}).

The maximal temperature reached within the micro-crack for a modulation at 2 GHz is higher than the maximal temperature in the unmodulated reference case, whereas it is the same for the 10 GHz modulation. Moreover, for time $t \leq 3$ ns, we observe that the temperature increases smoothly for the unmodulated pulse. For the 2 GHz modulation, the variation of temperature varies with a pseudo-period of 500 ps, which corresponds to the frequency of the AM. We notice the same behavior for the 10 GHz modulated pulse, but with a much lower amplitude. Absorption of the

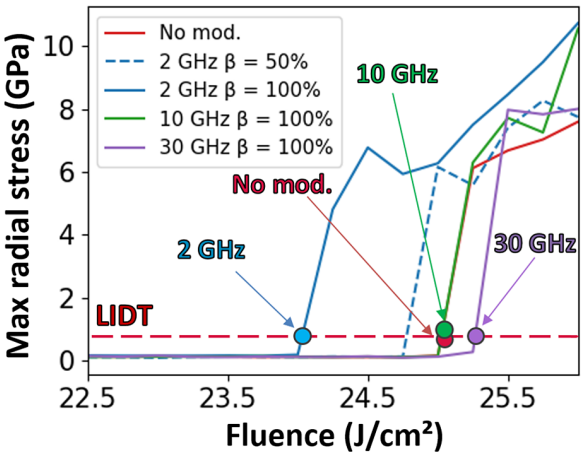

Figure 9. Evolution of radial stress with respect to laser fluence for different temporal modulations: 2 GHz with $\beta = 50\%$ or 100%, 10 GHz with $\beta = 100\%$ and 30 GHz with $\beta = 100\%$. Arrows point to the LIDT obtained for the reference without modulation (no mod.) as well as modulated pulses with $\beta = 100\%$.

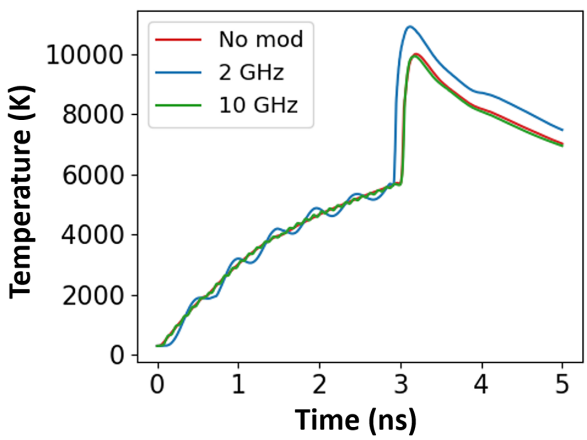

Figure 10. Evolution of the maximal temperature reached inside the micro-crack with respect to time for the unmodulated reference pulse and two modulated pulses at 2 and 10 GHz ($\beta = 100\%$).

https://doi.org/10.1017/hpl.2022.41 Published online by Cambridge University Press

amplitude modulated pulses acts as a 'low-pass' filter, at least for frequencies equal to or higher than 10 GHz.

4.4. Discussion of the simulated results

The simulations presented in this section are in good agreement with the experimental results presented in Section 2.3, as far as qualitative behavior is concerned. In particular, to this day, it is impossible to conclude the quantitative behavior of the impact of AM on LID.

One of the main limitations is that simulations and experiments do not express LID with the same metric. Indeed, simulations only show how one particular and arbitrary SSD behaves under laser irradiation. However, global LID behavior of the optical component, which is measured as damage densities, is a function of several SSDs of different natures (NBOHC, ODC, color center, residual slurry particles from polishing processes, etc.) and with different sizes and orientation parameters (width and angle of incidence with the beam). The fact that we used a single defect in our model might not be enough to assess the impact of FM-to-AM conversion on the LID of fused silica.

Even though the silica samples that were used to carry out experimental LID tests underwent similar polishing processes, the same experiment realized on a different sample can lead to dissimilar quantitative results. This is in fact what we observed on the samples polished by the THALES-SESO and ZYGO companies. In the case of LF versus HF modulations, the same trends were observed but for different fluence ranges and different magnitudes. It is as if the nature of the SSD between the different samples exhibited a different absorption dynamic to the incident laser pulse.

An extensive study was considered in one of the papers[4] that inspired our model. It was shown that it was possible to simulate an entire damage law for fused silica at 351 nm with initial defects of different characteristics. Although we only wanted to show trends regarding the impact of temporal shapes on a single damage, similar simulations could be implemented with different temporal shapes.

Finally, a more general critique can be expressed as far as the model is concerned. Modeling of LID with our model requires data about fused silica for significant temperature T and density ρ ranges. The SCAALP data that we use for the plasma phase are used to compute permittivity as well as thermal conductivity. The data we use for fused silica in the plasma phase, which are based on the mix of SCAALP data for oxygen and silicon, are far from ideal and surely lack consistency.

5. Conclusion

This work describes the impact of the temporal shape of nanosecond laser pulses on LID at 351 nm. Amplitude modulators installed on the MELBA experimental testbed were used to study the impact of FM-to-AM conversion on LID. Experimental data showed that AMs around 2 GHz lead to an increase in damage densities for a large fluence range, when compared to a reference unmodulated FIT pulse. Moreover, this difference in damage densities increases with the peak power of the laser pulse. However, when the modulation frequency is equal to or above 10 GHz, this difference is no longer observed and damage densities are the same as those of the unmodulated pulse, regardless of the peak power.

The 1D Lagrangian hydrodynamic code Esther allowed us to create a model for representing LID originating from a single absorbing defect. The model was validated by comparing our simulations with known experimental and simulated results found in the laser damage scientific literature[10]. Then, the model was used to run LID simulations with pulses like those used experimentally. We showed that the simulation and experiments are in good agreement, as far as qualitative behavior is concerned.

Finally, experiments were recently carried out on the MELBA experimental testbed to assess the impact of FM-to-AM conversion on the LID of thicker silica windows, more representative of the vacuum window found at the LMJ facility. The high peak power reached due to this phenomenon may lead to enhanced nonlinear propagation. The high peak power reached with temporal modulations can increase the Bespalov–Talanov gain for the Kerr effect, which typically leads to a local intensity increase and the enhancement of LID[25]. In the worst case, this increase might lead to the filamentation phenomenon inside the silica optic[26,27].

References

1. C. A. Haynam, P. J. Wegner, J. M. Auerbach, M. W. Bowers, S. N. Dixit, G. V. Erbert, G. M. Heestand, M. A. Henesian, M. R. Hermann, K. S. Jancaitis, K. R. Manes, C. D. Marshall, N. C. Mehta, J. Menapace, E. Moses, J. R. Murray, M. C. Nostrand, C. D. Orth, R. Patterson, R. A. Sacks, M. J. Shaw, M. Spaeth, S. B. Sutton, W. H. Williams, C. C. Widmayer, R. K. White, S. T. Yang, and B. M. Van Wonterghem, Appl. Opt. **46**, 3276 (2007).
2. J.-L. Miquel, C. Lion, and P. Vivini, J. Phys. Conf. Ser. **688**, 012067 (2016).
3. B. C. Stuart, M. D. Feit, A. M. Rubenchik, B. W. Shore, and M. D. Perry, Phys. Rev. Lett. **74**, 2248 (1995).
4. P. Grua, L. Lamaignère, M. Chambonneau, R. Courchinoux, and J. Néauport, Opt. Lett. **43**, 2692 (2018).
5. J. R. Murray, J. Ray Smith, R. B. Ehrlich, D. T. Kyrazis, C. E. Thompson, T. L. Weiland, and R. B. Wilcox, J. Opt. Soc. Am. B **6**, 2402 (1989).
6. J. E. Rothenberg, J. Opt. Soc. Am. B **14**, 1664 (1997).
7. J. E. Rothenberg, D. F. Browning, and R. B. Wilcox, Proc. SPIE **3492**, 51 (1999).
8. S. Hocquet, D. Penninckx, E. Bordenave, C. Gouédard, and Y. Jaouën, Appl. Opt. **47**, 3338 (2008).

https://doi.org/10.1017/hpl.2022.41 Published online by Cambridge University Press

9. T. Suratwala, L. Wong, P. Miller, M. D. Feit, J. Menapace, R. Steele, P. Davis, and D. Walmer, J. Non-Crystal. Solids **352**, 5601 (2006).
10. R. Diaz, M. Chambonneau, R. Courchinoux, P. Grua, J. Luce, J.-L. Rullier, J.-Y. Natoli, and L. Lamaignère, Opt. Lett. **39**, 674 (2014).
11. M. Veinhard, O. Bonville, R. Courchinoux, R. Parreault, J.-Y. Natoli, and L. Lamaignère, Proc. SPIE **10447**, 1044708 (2017).
12. L. Lamaignère, S. Bouillet, R. Courchinoux, T. Donval, M. Josse, J.-C. Poncetta, and H. Bercegol, Rev. Sci. Instrum. **78**, 103105 (2007).
13. L. Lamaingère, M. Balas, R. Courchinoux, T. Donval, J. C. Poncetta, S. Reyné, B. Bertussi, and H. Bercegol, J. Appl. Phys. **107**, 023105 (2010).
14. International Organization for Standardization, ISO 21254-1:2011 (2011).
15. M. Chambonneau, J.-L. Rullier, P. Grua, and L. Lamaignère, Opt. Express **26**, 21819 (2018).
16. R. Diaz, R. Courchinoux, J. Luce, C. Rouyer, J.-L. Rullier, J.-Y. Natoli, and L. Lamaignère, Appl. Phys. B **121**, 439 (2015).
17. M. Pfiffer, P. Cormont, E. Fargin, B. Bousquet, M. Dussauze, S. Lambert, and J. Neauport, Opt. Express **25**, 4607 (2017).
18. L. Skuja, J. Non-Crystal. Solids **239**, 16 (1998).
19. S. Laffite, S. D. Baton, P. Combis, J. Clerouin, M. Koenig, V. Recoules, C. Rousseaux, and L. Videau, Phys. Plasmas **21**, 082705 (2014).
20. K. Saito and A. J. Ikushima, Phys. Rev. B **62**, 8584 (2000).
21. C. W. Carr, J. D. Bude, and P. DeMange, Phys. Rev. B **82**, 184304 (2010).
22. C. Blancard and G. Faussurier, Phys. Rev. E **69**, 016409 (2004).
23. G. Faussurier, C. Blancard, P. Cossé, and P. Renaudin, Phys. Plasmas **17**, 052707 (2010).
24. H. Bercegol, P. Grua, D. Hébert, and J.-P. Morreeuw, Proc. SPIE **6720**, 41 (2007).
25. M. Veinhard, O. Bonville, S. Bouillet, E. Bordenave, R. Courchinoux, R. Parreault, J.-Y. Natoli, and L. Lamaignère, J. Appl. Phys. **124**, 163106 (2018).
26. H. Bercegol, L. Lamaignère, V. Cavaro, and M. Loiseau, Proc. SPIE **5991**, 613 (2006).
27. E. Feigenbaum, J.-M. G. D. Nicola, and J. D. Bude, Opt. Express **27**, 10611 (2019).

https://doi.org/10.1017/hpl.2022.41 Published online by Cambridge University Press